



# Formulation of promising antibacterial, anticancer, biocompatible and bioactive biomaterial as therapeutic drug delivery system for biologically active compound loaded on clay polymer

H. A. Fetouh<sup>1</sup> · H. Abdel-Hamid<sup>1</sup> · A. A. H. Zaghloul<sup>1</sup> · A. E. Ghadban<sup>1</sup> · A. M. Ismail<sup>1</sup>

Received: 1 February 2022 / Revised: 27 September 2022 / Accepted: 6 October 2022 /  
Published online: 1 November 2022  
© The Author(s) 2022

## Abstract

The synthesized heterocyclic compound: 5-[4-bromobenzylidene amino)-1, 3, 4-thiadiazole-2-thiol abbreviated as BATT possessed good antibacterial activity for various Gram-negative and Gram-positive bacteria. In addition to potent antitumor activity to breast cancer, for the first time, the novelty of this study is facile low-cost formulation of safe antitumor drug delivery system (DDS) for breast cancer from such simple heterocyclic compound. Heterocyclic compound is efficiently and spontaneously incorporated into MMT clay polymer matrix forming novel therapeutic nanocomposite DDS for breast cancer. BATT successfully intercalates MMT clay polymer matrix. Electron donation ability of nanocomposites is confirmed by cyclic voltammetry in terms of small peak-to-peak redox potential  $\Delta E_{\text{peak}}$ . Adsorption of BATT on clay is carried out by batch adsorption method. Better adsorption strength at low pH 2 decreased with increasing pH. Adsorption data are analyzed by multiple mathematical models. MMT clay is an efficient carrier polymer heterogenous adsorbent for BATT at optimum conditions: contact time 2.0 h, pH 2 and initial concentration up to 1200 ppm. Adsorption rate constant,  $k_2$  equals  $14.6 \times 10^{-3}$  and  $q_e$  19 mg g<sup>-1</sup> ( $R^2$  0.999). pH of zero charge of MMT at pH 3 reflected adsorption mechanism of MMT. At pH 2, BATT is loaded on MMT by physis- and chemisorption. At pH 4, BATT is loaded on MMT by chemisorption.

**Keywords** Drug delivery system · Heterocyclic compound · Clay polymer · Nanocomposites · Adsorption

---

✉ H. A. Fetouh  
howida\_fetouh@alexu.edu.eg

<sup>1</sup> Chemistry Department, Faculty of Science, Alexandria University, Alexandria, Egypt

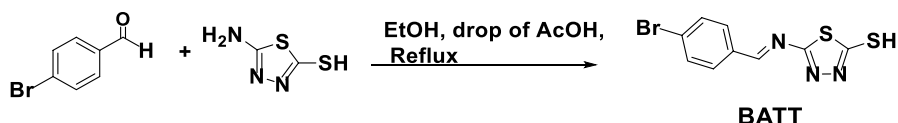
## Introduction

Nanocomposites drug delivery system (DDS) targeting therapeutic drug for treating cancer is a promising medicinal nanotechnology [1]. In current era of molecular medicine, much efforts have developed therapeutic DDS for breast cancer as nanocomposites of biomaterials [2]. Breast cancer, BC, represents quarter percent of cancer types. It is the second common cancer type that has a high incidence rate. Two million new cases of BC appear annually. It is among the main causes of women death. Most BC begins in breast tissue of glands lobules for milk production, or in ducts connecting lobules to nipple. Remainder breast is made up of fatty, connective and lymphatic tissues [3].

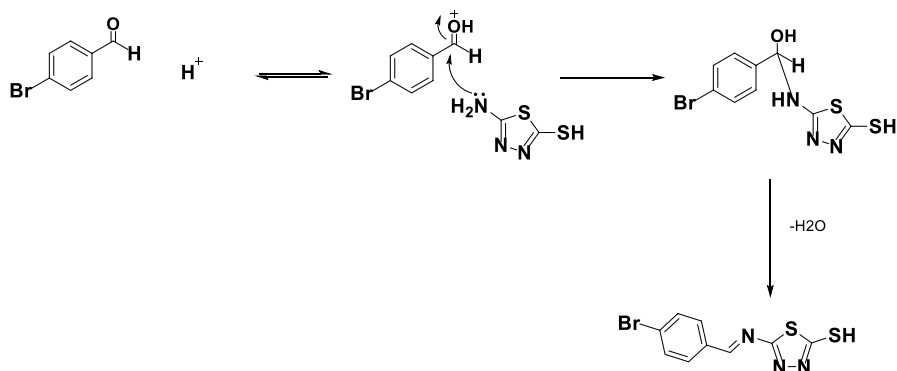
BC is caused by unhealthy lifestyles, long time fertility, using preventive pregnancy hormones and hormone replacement therapy, no children and breastfeeding, obesity after menopause, physical inactivity, alcohol consumption, family history, genetic predisposition and inherited mutations [3]. BC is treated by radiation therapy, targeted chemotherapy and endocrine hormone therapy. Chemotherapy (CT) harms human health by therapeutic antitumor drugs due to poor solubility in aqueous biological fluids, rapid deactivation, low apparent permeability and non-biodegradability [4]. Limitation of CT for BC is insolubility of therapeutic drugs in aqueous media [1]. DDS reduces drug side effects and maximizing drug action. DDS design is the most important nanotechnology. Therapeutic drug should possess high electron density for efficient loading on biocompatible polymer carrier [1]. MMT clay is a hydrated aluminosilicate inorganic polymers, mixed fine-grained clay minerals and metal oxides. MMT is safe drug carrier due to large specific internal surface area, physicochemical stability and several other structural and surface properties. MMT has high adsorption capacity, enhanced rheology, intercalate and reserve large neutral water-insoluble drug molecules into interlayer space 2D aluminosilicate layers. MMT releases incorporated loaded drugs in biological fluids via ion exchange mechanism or adsorption on porous active sites. MMT has high cation exchange capacity CEC for  $\text{Na}^+$  or  $\text{K}^+$  ions 1.0 mg equiv  $\text{g}^{-1}$ . 0.96 nm and 0.94 nm platelet thickness [1]. Mechanism of DDS formulation is mainly adsorption of therapeutic drug onto pores of MMT [5]. MMT is bioactive, biodegradable, hemocompatible and non-toxic [1]. Main objectives of study are preparation and characterization of new nanocomposites of biologically active 5-[4-bromobenzylidene amino]-1, 3, 4-thiadiazole-2-thiol (BATT) compound on bioactive MMT polymer. Compound BATT is selected for adsorption on clay inorganic polymer as it is biologically active compound for simulation new antibacterial and anticancer DDS.

## Materials and methods

All chemicals are of analytical grades obtained from Sigma-Aldrich used as received without further purification. BATT is prepared as follows [6]. 1.33 g (0.01 mol) solution: 5-amino-2-mercapto-1,3,4- thiadiazole, AMT, is dissolved



**Scheme 1** Synthesis route



**Scheme 2** Mechanism of synthesis BATT

in 25 mL absolute ethanol, treated with (1.45 g, 0.01 mol) *p*-bromobenzaldehyde solution dissolved in 25 mL ethanol. Three drops of glacial acetic acid is added dropwise. Mixture is heated under reflux for 6 h. Solid separated out upon cooling is filtered, dried and crystallized from EtOH/DMF as pale yellow crystals, 87% yield; m.p. 223 °C.

Chemical structure of BATT is confirmed using FTIR absorption vibrational bands (KBr): 2925(SH-); 1610(C=N); 1552 (C=C Ar-H); 1069 (C-N); 1036 (C-H); 825 (C-C-C bending in plane); 712 (C-S); 667.20 (C-Br); 539 (C-C-C bending out of plane). <sup>1</sup>H NMR (400 M Hz, DMSO-*d*<sub>6</sub>) at δ<sub>H</sub> (ppm): 13.0 (1 H singlet, SH group; 9.98 (1 H singlet, -CH=N); 7.80–7.07 (4 H multiple, aromatic protons); <sup>13</sup>C NMR (100 MHz, DMSO-*d*<sub>6</sub>) δ<sub>C</sub> 181.4; 162.1; 159.2; 132.8; 132.2; 131.8; 129.3; Anal. Cald: C<sub>9</sub>H<sub>6</sub>BrN<sub>3</sub>S<sub>2</sub> (300.187 g mol<sup>-1</sup>): C, 36.01; H, 2.02; N, 13.99; S, 21.36. Found: C, 36.00; H, 2.01; N, 13.89; S, 21.34.

It contains 5-membered heterocyclic thiadiazole nucleus, thiol group and Schiff base synergistically enhanced biological activity. BATT is prepared according to Scheme 1 via reflux *p*-bromobenzaldehyde with AMT in presence of acetic acid catalyst.

Formation mechanism is illustrated in Scheme 2. *p*-bromobenzaldehyde is protonated by acetic acid, attacking amino group of thiadiazole nucleus to carbonyl carbon affording iminol which consequently dehydrated by reflux to afford corresponding Schiff's base BATT.

BAAT and nanocomposites are characterized using: Fourier transform infrared (FTIR) spectroscopy, KBr disc, frequency range: 200–4000 cm<sup>-1</sup> using Bruker TENSOR 37 spectrophotometer, model 1430 calibrated by polystyrene film

( $1602 \pm 1 \text{ cm}^{-1}$ ), nuclear magnetic resonance  $^1\text{H}$  NMR and  $^{13}\text{C}$  NMR, Bruker spectrometer (400 MHz). Chemical shift ( $\delta$  ppm) is relative to TMS internal standard. m.p. is determined with a Mel-Temp. apparatus and uncorrected. TLC is performed on Baker-Flex silica gel 1B-F plates using ethyl acetate-petroleum ether eluent (1:1v/v); elemental microanalysis; powder X-ray diffraction, pXRD using X-ray Shimadzu XRD-6100 diffractometer; thermogravimetric analysis TGA, differential thermogravimetric; and differential thermal analysis DTA using Shimadzu DTG 60H thermal analyzer in platinum crucible at temperature range 20–700 °C under nitrogen and heating rate 10 °C/min. [7, 8].

In vitro antibacterial activity tests at 30 °C using diffusion agar method, well 6.0 mm diameter: 100  $\mu\text{L}$  BATT and ciprofloxacin standard antibiotic. Tested strains are obtained from culture collection Regional Center for Mycology and Biotechnology, Al-Azhar University, Cairo, Egypt). Tested Gram-positive,  $G^+$  (*Staphylococcus aureus*, *E. coli*) and Gram-negative bacteria,  $G^-$  (*Pseudomonas aeruginosa*, *Bacillus cereus*) are cultured on nutrient agar. Antibacterial activity was determined after one day by cut-plug method [8].

Some parameters of optimized structure are calculated by B3LYP/6 method, basis set 31-G *d*, *p* level using GAUSSIAN 9 package software, frontier molecular orbitals, HOMO and LUMO are visualized with Gaussian view [10]. Some chemical descriptors are calculated [7]:

$$\text{Ionization potential } (I) = -E_{\text{HOMO}}, \text{ electron affinity } (A) = -E_{\text{LUMO}} \quad (1)$$

$$\text{Absolute electronegativities, } \chi = -\frac{(E_{\text{LUMO}} + E_{\text{HOMO}})}{2} \quad (2)$$

$$\text{Chemical potentials, } \text{Pi} = -\chi \quad (3)$$

$$\text{Absolute hardness, } \eta = \frac{E_{\text{LUMO}} - E_{\text{HOMO}}}{2} \quad (4)$$

$$\text{Absolute softness, } \sigma = \frac{1}{\eta} \quad (5)$$

$$\text{Global softness, } S = \frac{1}{2\eta} \quad (6)$$

$$\text{Global electrophilicity, } \omega = \frac{\text{Pi}^2}{2\eta} \quad (7)$$

$$\text{Global hardness } \eta = \frac{I - A}{2} \tag{8}$$

Redox characteristic of BATT is clarified via cyclic voltammetry from 0.5 V to − 0.5 V, scan rate 20 mV s<sup>−1</sup> using silver–silver chloride reference electrode. Sample is loaded on glassy carbon electrode 0.032 cm<sup>2</sup> surface area [9].

BATT is uploaded on clay polymer by adsorption to formulate antibacterial anticancer DDS. In batch adsorption method, adsorption parameters contact time, pH and initial concentration are optimized. For determination maximum adsorption capacity, 100 mg MMT is dispersed in 20 mL de-ionized water contains 15 mg BATT, agitated at room temperature for different contact time (*t*) up to 3.5 h. Mixture is centrifuged and filtered using poly tetra-fluoro-ethylene (PTFE) filter, 0.25 μm pore size. Residual concentration in supernatant is determined by UV–Vis spectroscopy at λ<sub>max</sub>. 320 nm [10]. Each adsorption run is carried out in triplicate (*n*=3). Average value is calculated along with standard deviation.

$$\text{Adsorbed amount } qt = \frac{(C_0 - C_e)V}{m, g} \tag{9}$$

where *qt* is adsorbed quantity mg g<sup>−1</sup>, C<sub>0</sub> is initial concentration mg L<sup>−1</sup>, C<sub>e</sub> is equilibrium concentration, mg L<sup>−1</sup>, *m* is mass adsorbent, *V* is solution volume, *L*.

$$\text{Percent adsorption } \% A = \frac{(C_0 - C_e)}{C_0} \times 100 \tag{10}$$

To optimize pH, 100 mg MMT is treated with 20 mL 15 mg BATT solution at pH range 2–12. pH is adjusted using aqueous solutions 0.1 M NaOH or 0.1 M HCl. To optimize initial concentration, 100 mg MMT is mixed with 10 mL BATT solution containing different ppm concentration BATT.

All adsorption data are carried out in triplicate (*n*=3) for calculation *qt* and % adsorption. All data are represented as mean  $\bar{x}$  and S.D

$$\text{Average mean : } \bar{x} = \frac{\text{Sum of observations } \sum x}{\text{number of observations, } n} \tag{11}$$

$$\text{Standard deviation (S.D.)} = \sqrt{\frac{\sum x^2 - \frac{(\sum x)^2}{n}}{n - 1}} \tag{12}$$

In regression analysis for any two variables *X*, *Y*

$$\text{Mean squared error (MSE)} = \frac{1}{n} \sum_{i=1}^n (Y_i - \hat{Y}_i)^2 \tag{13}$$

where *n* is the number of data points, *Y<sub>i</sub>*, ...,  $\hat{Y}_i$  are observed and predicted values, respectively. MSE is calculated from a set *X* and *Y* by finding regression line, insert *X* values into linear regression equation to find  $\hat{Y}_i$ .

To find the best thermodynamic or kinetic model for adsorption data, an error analysis is performed. Sum of squares errors (SSE) and chi-square ( $\chi^2$ ) are achieved by equations:

$$\text{SSE} = \sum_{i=1}^n (q_{e \text{ exp}} - q_{e \text{ cal}})^2 \quad (14)$$

$$\chi^2 = \sum_{i=1}^n \frac{(q_{e \text{ exp}} - q_{e \text{ cal}})^2}{q_{e \text{ cal}}} \quad (15)$$

where  $q_{e \text{ exp}}$  and  $q_{e \text{ cal}}$  are experimental and predicted adsorption capacities at equilibrium, respectively.

Nanocomposite NC<sub>1</sub> is prepared [1]: An aqueous MMT dispersion (1% w/v) is prepared by dispersing 2.0 g MMT in 200 mL double distilled water. Turbid dispersion is left at room temperature for eighteen hrs. for complete swelling. At pH 4.0 of dispersion, 0.2778 g BATT equivalent to excess three CEC of MMT is dissolved in 50 mL DMF and added to MMT dispersion. Mixture is stirred for 4.0 h at 40 °C, left for settling for 18 h at room temperature then filtered. Precipitate washed several times with DMF to remove unbound BATT molecules, dried at room temperature, grinded with mortar and pestle to be fine powder [13]. NC<sub>2</sub> is prepared by the same method of NC<sub>1</sub> at pH 2.

Colloidal stability of NC<sub>1</sub> is confirmed using NanoZS/ZEN3600 Zetasizer (Malvern, Instruments Ltd, Malvern, UK) to determine zeta potential [11].

## Results and discussion

All spectral analysis in Fig. 1a–c confirmed chemical structure of BATT. IR spectrum showed characteristic vibrational bands at wavenumber, cm<sup>-1</sup>: 2925 (SH-); 1610 (C=N); 1552 (C=C Ar-H); 1069 (C-N); 1036 (C-H); 825 (C-C-C bending in plane); 712 (C-S); 667.20 (C-Br); 539 (C-C-C bending out of plan) [1].

<sup>1</sup>H NMR spectrum (400 MHz, DMSO-d<sub>6</sub>) showed a singlet at  $\delta$  13.0 ppm (SH group); a singlet at 9.98 (–CH=N); aromatic protons multiplet at 7.80–7.07 ppm. <sup>13</sup>C (DMSO-100 MHz);  $\delta$ : 181.4; 162.1; 159.2; 132.8; 132.2; 131.8; 129.3. Protons and carbons of BATT molecules are shown in their appropriate positions [12].

BAAT showed potent antibacterial to G<sup>-</sup> bacteria than ciprofloxacin and moderate activity to G<sup>+</sup> bacteria, Table 1.

Antibacterial effect of BATT is more pronounced against G<sup>-</sup> bacteria (Fig. 2) than G<sup>+</sup> bacteria that possess thick cell wall contains massive peptidoglycan. G<sup>-</sup> bacteria have two layers cell membranes, and outer membrane comprises lipopolysaccharide protective against antibiotics and antibacterial drugs and detergents that could damage inner membrane or cell wall peptidoglycan [8]. IZ for BATT exceeds that of Ciprofloxacin for G<sup>-</sup> bacteria.

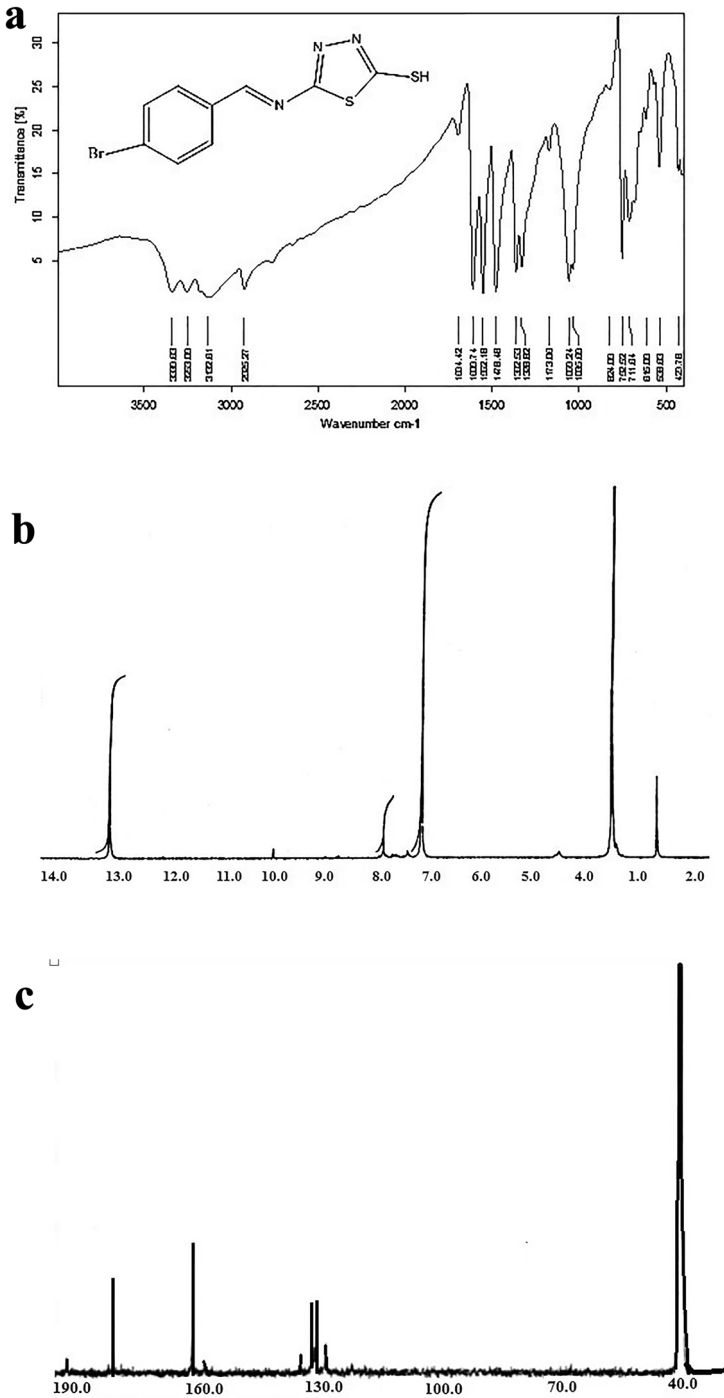
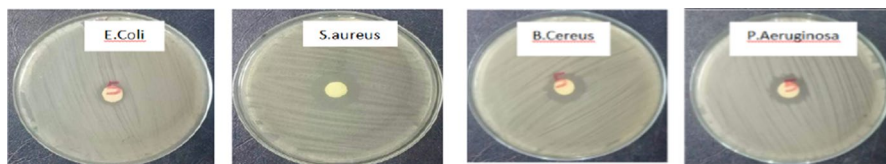


Fig. 1 FTIR, <sup>1</sup>H NMR and <sup>13</sup>C NMR spectra of MMT, respectively

**Table 1** Inhibition zone (IZ) diameters

Bacteria microorganism species	G <sup>+</sup>		G <sup>-</sup>	
	<i>S. aureus</i>	<i>E. coli</i>	<i>P. aeruginosa</i>	<i>B. cereus</i>
	Inhibition zone-diameter (mm)			
BATT	24	14	18	20
Ciprofloxacin antibiotic	34	31	14	19

**Fig. 2** IZ for bacteria using BAAT

SRB assay in-vitro antitumor activity of BATT is evaluated by monitoring cytotoxicity via comparison between bioavailability McF-5 normal human lung fibroblast and cancer cells lines: McF-7 breast, CACO intestinal colon and liver HepG-2 [1]. Cell lines are sub cultivated, for 120 passages plated in 96-multiwell plate  $10^4$  cells/well along one day for fixation on plate walls before adding 0, 1, 2.5, 5 and 10  $\mu\text{g}/\text{mL}$  BATT. Each dose is added to cell monolayer triplicates wells, incubated for two days at 37 °C under 5%  $\text{CO}_2$  atmosphere. Cells are fixed, washed and stained with sulfo-rhodamine-B stain. Excess stain is washed with acetic acid and attached stain is recovered by Tris EDTA buffer. Color optical density (O.D.) is measured in Mindray MR-96A ELISA reader at 570 nm. Plot surviving fraction-concentration gave survival curve of each treated tumor cell.  $\text{IC}_{50}$  percent control of infected and uninfected response values is calculated for BATT and Doxorubicin positive standard. Method validation is tested by taking fourfold concentration of blank and control.

Table 2 shows mean  $\bar{x}$  and standard error  $\overline{\text{SE}}$  or S.D. triplicates O.D, for each test solution in mean following Poisson distribution [13]. % viability of tumor and normal cells are determined in triplicates for each concentration, Table 2.

Table 3 collected mean values  $\bar{x}$  and  $\overline{\text{SE}}$  of %cell viability at different concentrations.

Small error  $\overline{\text{SE}}$  in mean value  $\bar{x}$  of tested concentrations confirmed validity and precision of SRB assay method.

Figure 3 shows BATT cytotoxicity to McF-7 cells and McF-5.

Error bars in histogram of cell viability versus concentration (Fig. 3) are due to small S.D. in triplicate data and confirmed high accuracy and precision of SRB assay.

BAAT inhibited availability of McF-7 by 14% at 31.25 mg/L and 15.6 mg/L with low cytotoxicity on normal cells McF-5 [13, 14]. It acts by heterocyclic rings and thiol group. It is recommended to formulation of DDS for BC using MMT safe



**Table 2** Statistical analysis of dependence of viability of cancer cells on concentration  $\bar{x}$  are 0.003, 0.229 and SE (0.001, 0.001) for B, C respectively

Concentration	HA CACO		HA HepG-5		HA McF-7		HA McF-5	
	O.D	%Viability	O.D	%Viability	O.D	%Viability	O.D	%Viability
250	0.011	3.44	0.015	5.21	0.01	3.44	0.013	4.32
250	0.012	3.88	0.016	5.65	0.01	3.44	0.015	5.21
250	0.014	4.77	0.012	3.88	0.02	5.21	0.012	3.88
125	0.112	48.23	0.118	50.89	0.12	50.44	0.127	54.87
125	0.111	47.78	0.119	51.33	0.12	49.56	0.125	53.99
125	0.116	50.00	0.117	50.44	0.12	50.00	0.124	53.54
62.5	0.138	59.76	0.141	61.09	0.13	53.99	0.149	64.63
62.5	0.137	59.31	0.136	58.87	0.13	54.44	0.151	65.52
62.5	0.132	57.10	0.142	61.53	0.12	52.21	0.152	65.96
31.25	0.156	67.74	0.151	65.52	0.15	63.30	0.178	77.49
31.25	0.153	66.41	0.161	69.96	0.15	63.74	0.176	76.60
31.25	0.149	64.63	0.171	74.39	0.15	64.63	0.181	78.82
15.6	0.212	92.57	0.225	98.34	0.19	82.37	0.221	96.56
15.6	0.217	94.79	0.224	97.89	0.19	83.70	0.223	97.45
15.6	0.216	94.35	0.221	96.56	0.20	86.36	0.233	101.88

Concentration	Blank (B)	Control (C)	HA-CACO	HA-HepG-2	HA-McF-7	HA-McF-5
<i>Cells viability</i>						
250	0.006	0.229	0.0123	0.014	0.012	0.013
125	0.005	0.228	0.113	0.118	0.116	0.125
62.5	0.001	0.227	0.135	0.139	0.124	0.150
31.5	0.001	0.231	0.152	0.161	0.147	0.178
15.6	0.0009	0.230	0.215	0.223	0.193	0.225

**Table 3** Statistical results of BATT adsorption on MMT

CACO	250	125	62.5	31.25	15.6	HEPG-5	125	62.5	31.25	15.6
$\bar{x}$	4.03	48.67	58.72	66.26	93.90	$\bar{x}$	50.00	60.50	63.90	97.60
$\overline{SE}$	0.39	0.678	0.828	0.90	0.68	$\overline{SE}$	0.26	0.68	2.56	0.53
McF-7	250	125	62.5	31.25	15.6	HA McF-5	250	125	62.5	31.25
$\bar{x}$	4.03	50.00	53.55	63.90	84.15	$\bar{x}$	4.47	54.14	65.37	77.64
$\overline{SE}$	0.59	0.26	0.68	0.39	1.17	$\overline{SE}$	0.39	0.39	0.39	0.64

adsorbent carrier. BATT IC50 at 11  $\mu\text{g/mL}$  is a comparable value to that of Doxorubicin, 8  $\mu\text{g/mL}$  [16].

Efficient BATT loading on MMT matrix is confirmed from FTIR vibrational bands at characteristic frequency,  $\text{cm}^{-1}$  (Fig. 4). MMT: 3445.82 (OH); 1637.55 (Si=O); 1049.97 (C-O stretching); 798.28 (Si-Si); 526.24 (Si-O); 468.32 (Al-O).

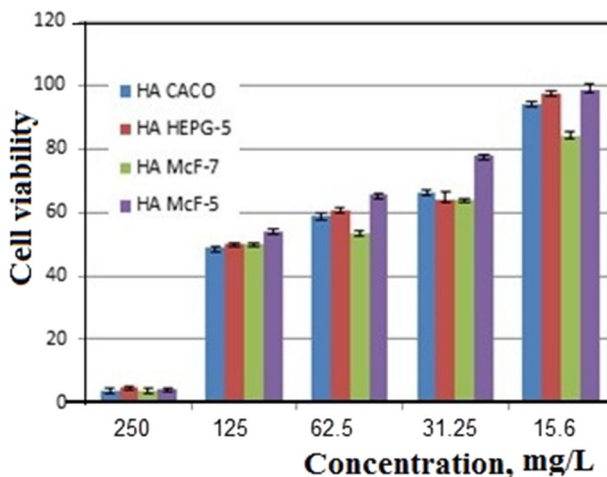


**Fig. 3** Histogram cell bio availability-concentration

$\text{NC}_1$ : 3441.22 (N–H); 1659.63 (Si=O); 1496.35 (C=S); 1439.03 (C–N); 1390.46 (CH=); 1048.15 (C–H); 795.13 (C–C–C bending in plane); 667.20, (C–Br); 524.63 (C–C–C bending out of plane); 467.52 (Al–N)  $\text{cm}^{-1}$ . New bands at 1659.63 (Si=O); 1496.35 (C=S); 1439.03 (C–N); 1390.46 (CH=); 667.20 (C–Br) or (Al–N) confirmed BATT adsorption on MMT. Bands at 3253.09, 3132.60, and 2925.27 symmetric stretching vibration of NH disappeared in  $\text{NC}_2$  [1].

Figure 5 shows optimized 3D geometrical structure of BATT. Computations are converged upon true minimum energy – 1120 eV ensuring stable ground state. High dipole moment 17.38 Debye reflected polarity charge separation and dielectric character of BAAT electron donor Lewis base.

Figure 6 shows wave functions  $\psi$  of electron density in molecular orbitals of BATT molecule in duplicate due to trans and cis isomers.  $\psi_{\text{HOMO}}$  lies on thiadiazole ring and  $\psi_{\text{LUMO}}$  on phenyl ring containing vacant *p*-orbitals [7].

Geometrical parameters atomic Mulliken charge reflecting electron density on atoms, bond lengths, bond angles and dihedral angles confirming molecular structure of BATT and dihedral angle are collected in, supplementary information SI, Table SI.1, 2. [1]. BATT is electrically neutral, stoichiometric formula  $\text{C}_9\text{H}_6\text{N}_3\text{S}_2\text{Br}$ . N13 has highest charge and it is electron donating site. C–H bond length is 1.1 Å. C–C bonds in phenyl group have same bond length 1.4 Å. C–N bond length, 1.3 Å is shorter than C–C bond due to electronegative N atom. Bond angles  $120^\circ$  confirmed trigonal planar  $\text{sp}^2$  hybridization. Dihedral angles  $\pm 179^\circ$  are for distorted linear  $\text{sp}^2$  hybridization. Bond angles less than  $90^\circ$  reflect distorted tetrahedral  $\text{sp}^3$  hybridization. Dihedral angles  $\pm 180^\circ$  are due to SP hybridization and molecular planarity. Dihedral angles  $180^\circ$ – $0^\circ$  suggested anti- and syn positions, respectively. Dipole moment on Cartesian coordinates is  $\mu_x$  3.7161,  $\mu_y$  – 2.7634,  $\mu_z$  – 0.4974. Electron transfer occurs from HOMO BATT into LUMO MMT [1, 7] (Fig. 7).

States per energy interval at each energy level available for electrons occupation density of states, DOS, and Fermi levels are viewed using Gauss Sum 2.2.5

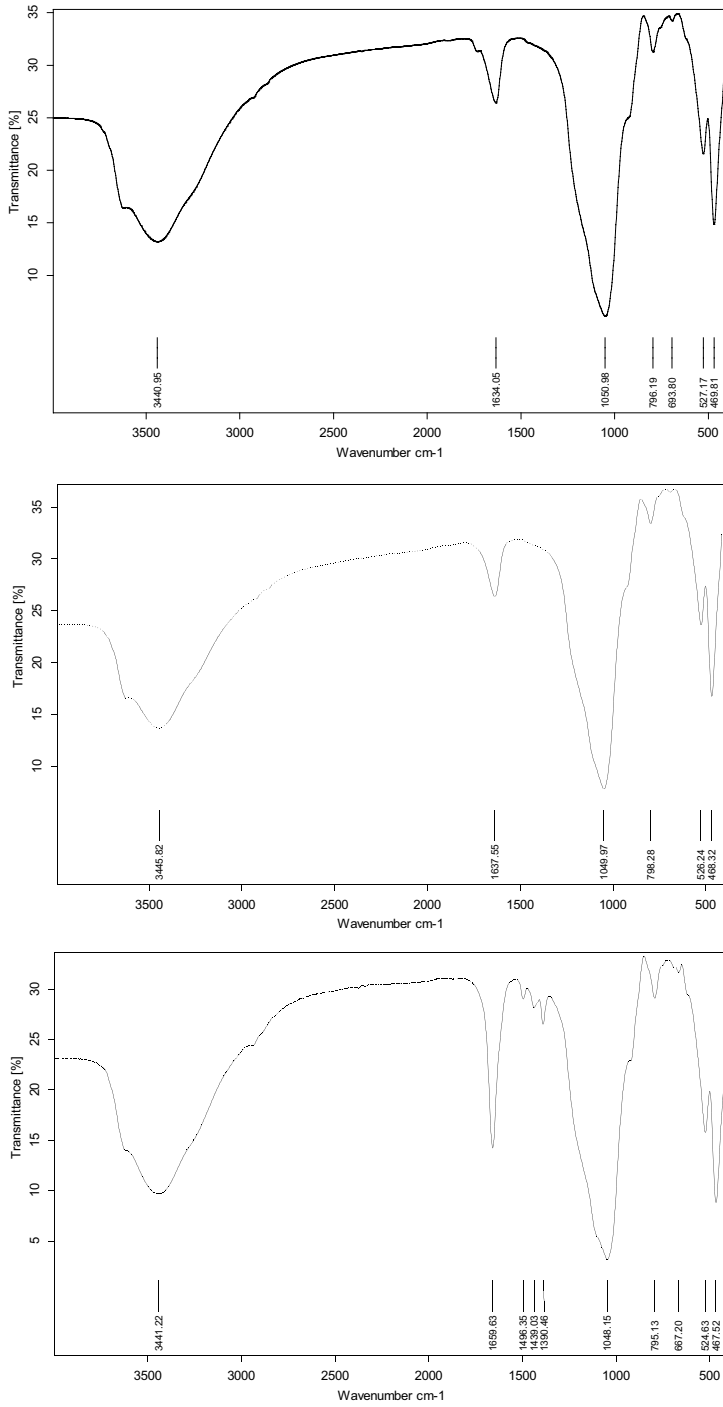


Fig. 4 FTIR spectra for MMT, NC<sub>1</sub> and NC<sub>2</sub> respectively

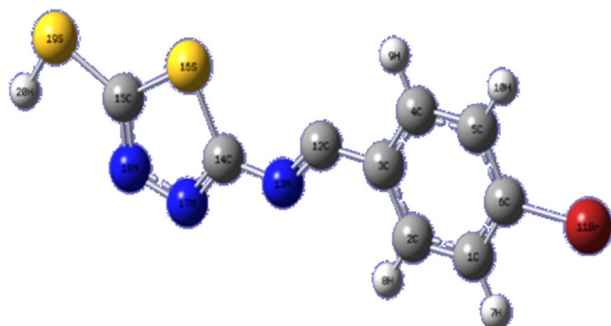


Fig. 5 Optimized geometry

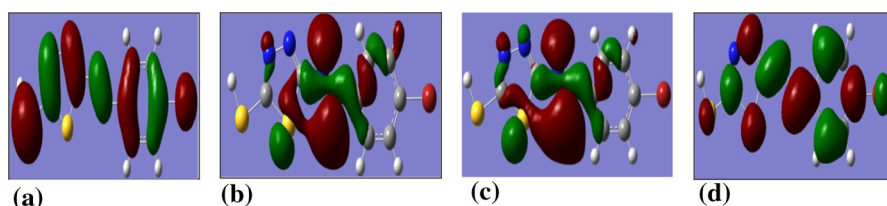


Fig. 6  $\psi$ : a  $\alpha$ -HOMO, b HOMO- $\beta$ , c One MO above HOMO- $\beta$ , d LUMO

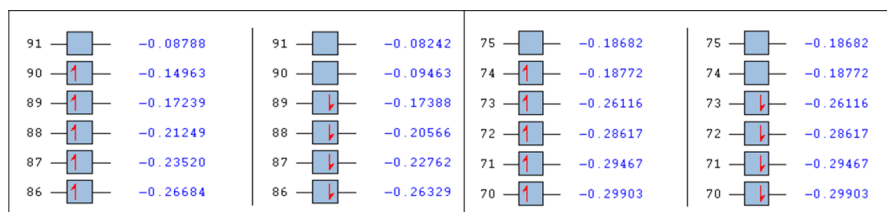


Fig. 7 HOMO energy level diagram BATT and NC<sub>1</sub>, respectively

program. Intense green colored DOS reflects many states available for electrons occupation and intense electron density [15] (Fig. 8).

Some molecular chemical activity indices are calculated based on  $E_{\text{HOMO}}$  and  $E_{\text{LUMO}}$ . Chemical potential,  $\mu$ ; electronegativity,  $\chi$ ; global hardness,  $\eta$ ; softness,  $\sigma$  and global electrophilicity index,  $\omega$ , are collected in Table 4. Electron donation ability of BATT to an appropriate acceptor sites is confirmed as  $\eta$  nearly equals  $\Delta E_{\text{LUMO-HOMO}}$  (band gap  $E_g$ ) indicating charge transfer from BATT molecule. Softness confirmed polarizability and inversely proportional to  $\eta$ . Parameters  $E_{\text{HOMO}}$ ,  $E_{\text{LUMO}}$  and  $\Delta E_{\text{LUMO-HOMO}}$  reflected electron donation ability of BAAT [7].

Small  $E_g$  0.1408 eV showed BATT is polarizable soft Lewis base. Adsorption center SH group chelates MMT clay via coordinate bond formation reinforced by back donation to vacant  $p$ -orbital in phenyl group. High  $E_{\text{HOMO}}$  indicated low ionization potential and high electron donation tendency to Al atoms in MMT with low

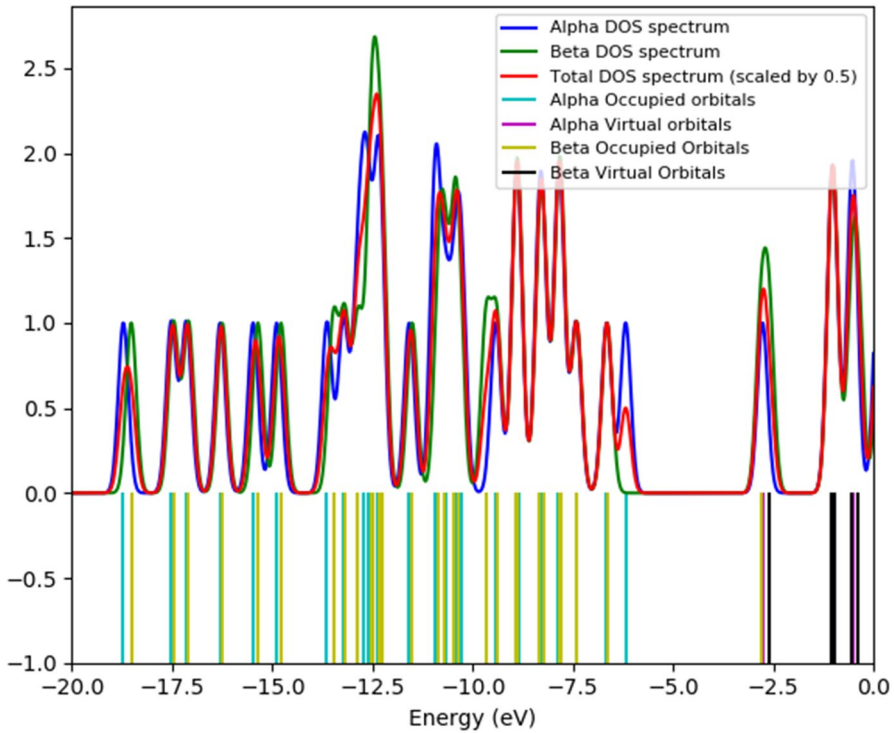


Fig. 8 DOS of BATT

Table 4 Reactivity descriptors, eV of BATT

$-E_{\text{HOMO}}$	$-E_{\text{LUMO}}$	$E_g$	$I$	$A$	$\chi$	$-\text{Pi}$	$\eta$	$\sigma$	$\omega$
0.1496	0.0878	0.1408	0.1496	0.0878	0.1187	0.1187	0.0308	32.46	0.0002

energy vacant *p*-orbital in MMT. Low  $E_{\text{LUMO}}$  indicated stronger electron accepting ability by back donation. Electrophilicity  $\omega$  measures stabilization by additional electronic charge [13]. Negative chemical potential, Pi, reflects stable molecular structure.

Redox characteristics of BATT and NCs are illustrated in Fig. 9.

NC<sub>1</sub> showed the smallest band gap,  $E_g$  peak-to-peak redox potential  $\Delta E_{\text{peak}}$ . Electron confinement enabled electron transfer from HOMO BATT to lower partially empty *p*-orbitals of Al atoms in MMT. NC<sub>1</sub> showed the best redox characteristics [16].

In Fig. 10 TEM micrographs showed NPs in NC<sub>1</sub> are well dispersed. Particles size ranged from 22 to 39 nm. MMT clay inorganic polymer has amorphous morphology continuous nanoscale polymeric sheets of slightly defined NPs. NC<sub>2</sub>

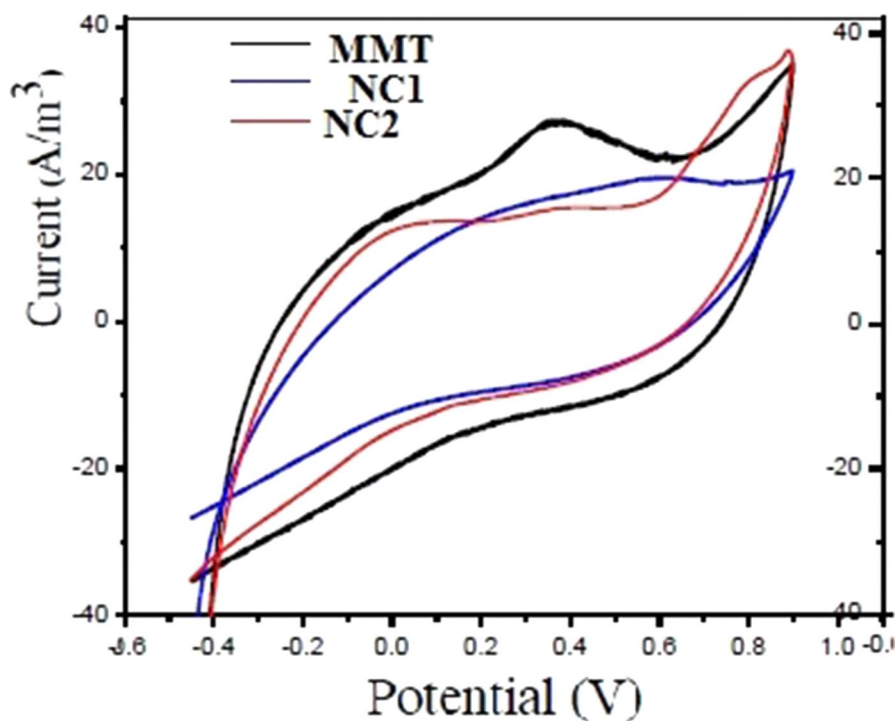


Fig. 9 Cyclic voltammograms

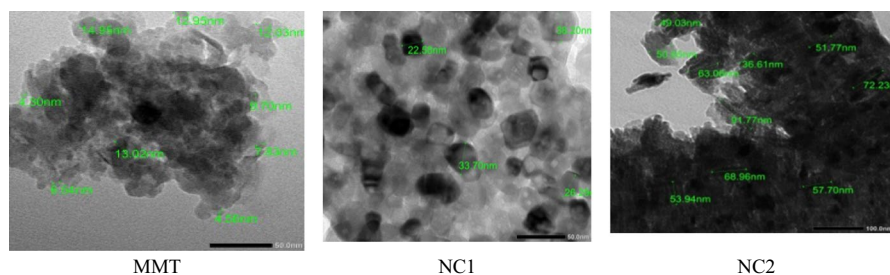


Fig. 10 TEM micrographs

had tree-like morphology and large particle size 36–91 nm more aggregated than  $NC_1$ .

Small particle size of  $NC_1$  confirmed large surface area/volume ratio and high Lewis basicity. Larger particle of  $NC_2$  indicated irreversible phase transition to more stable state and unsuitable DDS. It is excluded from further investigation.

Colloidal stability  $NC_1$  is established from negative zeta-potential  $-26.9$  mV [8] (Fig. 11).

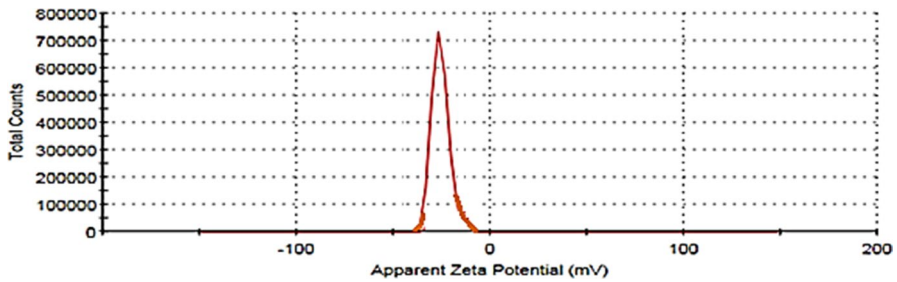


Fig. 11 Zeta potential of NC<sub>1</sub>

Negative charges on NC<sub>1</sub> protected nanoparticles against coagulation.

PXRD patterns in Fig. 12 confirmed existence of NC<sub>1</sub> as small suspended NPs showed fine wider diffraction peaks than NC<sub>2</sub> [17] as confirmed by crystal data.

Table SI.3 collected crystalline parameters: peak position of Miller indices  $h k \uparrow$ , interplanar distance ( $d$ ) both experimental and calculated.

Validity of pdF cards used to simulate pXRD patterns is confirmed through calculation interplant distance,  $d$ , diffraction angle,  $2\theta$  and  $h k \uparrow$  using check cell software program. Average crystalline size is calculated using Debye Scherer equation using the most intense peaks: Average particle size of NC<sub>1</sub> and NC<sub>2</sub> is 32 nm and 65 nm, respectively, in good agreement to those obtained from TEM micrographs. Weak intense XRD peaks of NC<sub>1</sub> confirmed nanocrystalline size with large surface area/volume ratio. NC<sub>2</sub> revealed moderate higher crystallinity than NC<sub>1</sub>. Structure type, geometry, crystal parameters and lattice parameters are shown in Table 5 using crystallography open database, COD, which agrees well with experimental pXRD patterns.

TGA plots related weight loss of BATT and NC<sub>1</sub> samples on heating (Fig. 13, Table 6).

DTA plots: temperature difference between tested and reference sample versus heating temperature,  $t$  °C (Fig. 14).

Activation energy,  $E_a$ , of decomposition and thermodynamic of thermal decomposition are calculated [5], SI.2. Arrhenius type plots are represented in Fig. SI.1 for decomposition steps. Table 7 demonstrates these parameters.

Nonlinear fitting in Fig. 15 showed optimizing adsorption parameters. Nonlinear plots of % adsorbed are obtained on optimizing time, pH and initial concentration. Figure 16a: Adsorption is very fast at start and adsorption equilibrium is established rapidly. Adsorption% is limited up at 2 h. equilibrium time for completion adsorbed layer.

Small error bars ( $\pm$  error) confirmed accuracy of batch adsorption method on BATT on MMT. Adsorption was very fast and equilibrium is established within 2.0 h when adsorbed amount is limited with optimum pH 2 and initial concentration up to 1200 ppm for maximum adsorption MMT.

To clarify behavior of BATT, data are analyzed using several adsorption isotherms Langmuir, Freundlich, Tempkin, Dubinin–Radushkevich, D–R, Halsey,

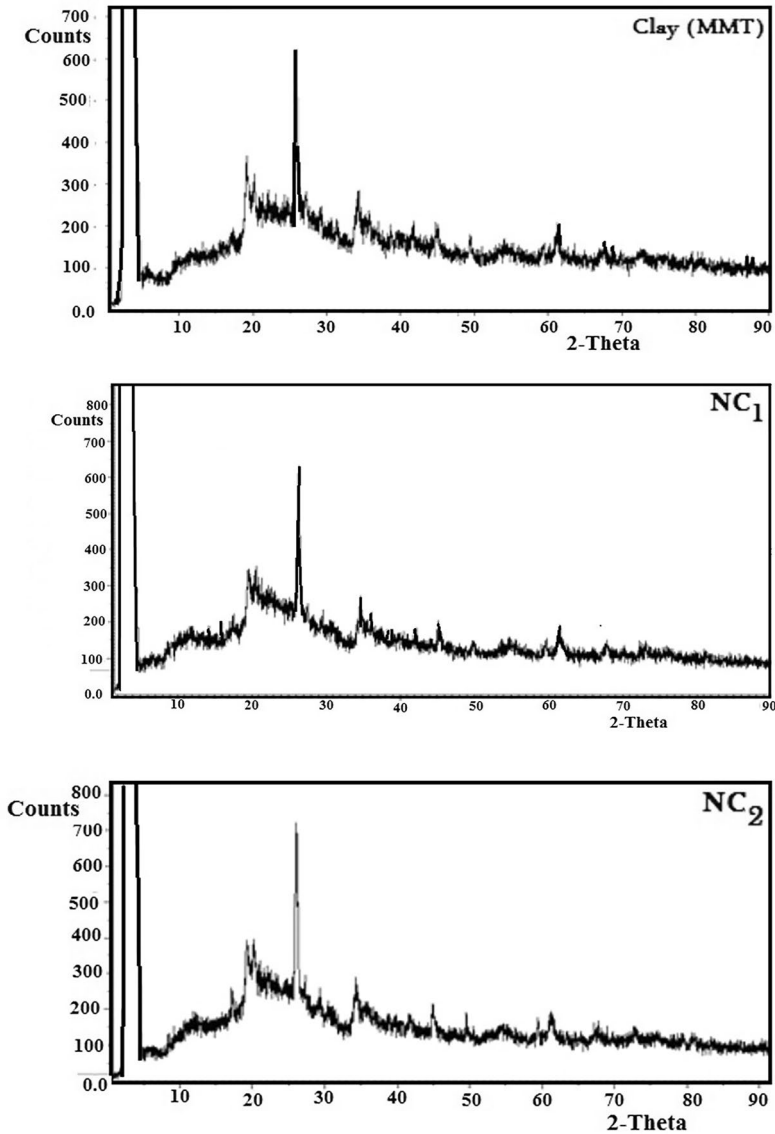


Fig. 12 pXRD MMT, NC<sub>1</sub> and NC<sub>2</sub>, respectively

Elovich and Harkins–Jura. Empirical equations are described in SI.2. Linear regression analysis is followed in linear fitting of adsorption data [18]. High value of error functions and low value of correlation coefficients ( $R^2$ ) for adsorption or kinetic model indicate that this model is not fitted to adsorption isotherm [19].

Adsorption parameters are collected in Table 8.

Adsorption data did not obey Langmuir and Harkins–Jura adsorption. Linear fitting of adsorption data to Freundlich adsorption isotherm confirmed multilayer



**Table 5** Lattice parameters

Parameter	MMT	NC <sub>1</sub>	NC <sub>2</sub>
PDF card COD	80–1387	08–0415	51–2072
Crystal system	Hexagonal		Monoclinic
Space group	P6222 (180)	P63/mmc (194)	P2/n (13)
Lattice parameters	$a=b=5.08600$ , $c=5.50900$ $\alpha=\beta=\gamma=90^\circ$ , $Z=1$	$a=b=2.46400$ , $c=6.73600$ $\alpha=\beta=\gamma=90^\circ$ , $Z=4$	$a=8.84000$ , $b=26.500$ , $c=8.060$ $\alpha=\gamma=90^\circ$ , $\beta=102.2^\circ$ , $Z=1$
Volume, Å <sup>3</sup>	123.41	35.42	1845.42

Volume of unit cell of NC<sub>2</sub>, 1845.42 Å<sup>3</sup> larger confirmed supra-molecular structure of NC<sub>2</sub> [17]

adsorption on heterogeneous surface. Heat of adsorption decreases linearly with increase surface coverage due to adsorbate–adsorbent interactions.  $R^2$  is high for D.R. model indicating suitability to describe adsorption of BATT on to MMT.

MSE is inversely proportional to correlation coefficient  $R^2$ . Low value MSE and high  $R^2$  for D.R. model indicate best fitting to adsorption data.

Kinetic of adsorption informed about adsorption rate and mechanism. Adsorption data are linearly fitted to kinetic parameters pseudo-first-order-, pseudo-second-order and Elovich kinetics models. Empirical equations are shown in SI.3.

Figure 16 Variation of adsorbed amount at any time  $t$  ( $qt$ ) versus  $t$ .

$qt$  showed rapid increase with time and then  $qt$  becomes limited at 2.0 h. contact time. MMT clay intercalated large neutral (BATT) molecules into interlayer space of 2D alumina-silicate layers.

Adsorption data are best fitted to pseudo-second-order kinetic model ( $R^2$  0.999) suggesting physisorption of BATT [10]. Figure 17 shows plot  $t/q$  versus  $t$  for pseudo-second-order kinetic. Kinetic parameters  $K_2$ ,  $q_e$  are obtained from slope and intercept of the obtained straight line (Table 9).

**Table 6** TGA of BATT and NC<sub>1</sub>

Sample	Step	Temp. range °C	Wt.loss %	
			Found	Cal
BATT	1	38.9–165.4	0.41	0.41
	2	165.4–324.5	8.59	8.58
	3	324.5–670.1	7.23	7.21
NC <sub>1</sub>	1	33.6–132.9	1.26	1.25
	2	132.9–217.1	1.49	1.48
	3	217.1–379.3	0.48	0.47
	4	379.3–699.0	0.76	0.75

Wt. loss NC<sub>1</sub> 17.88 mg to 13.89 mg lower than BATT, 16.50 mg to 0.31 mg indicating NC<sub>1</sub> is better thermally stable than BATT [8]

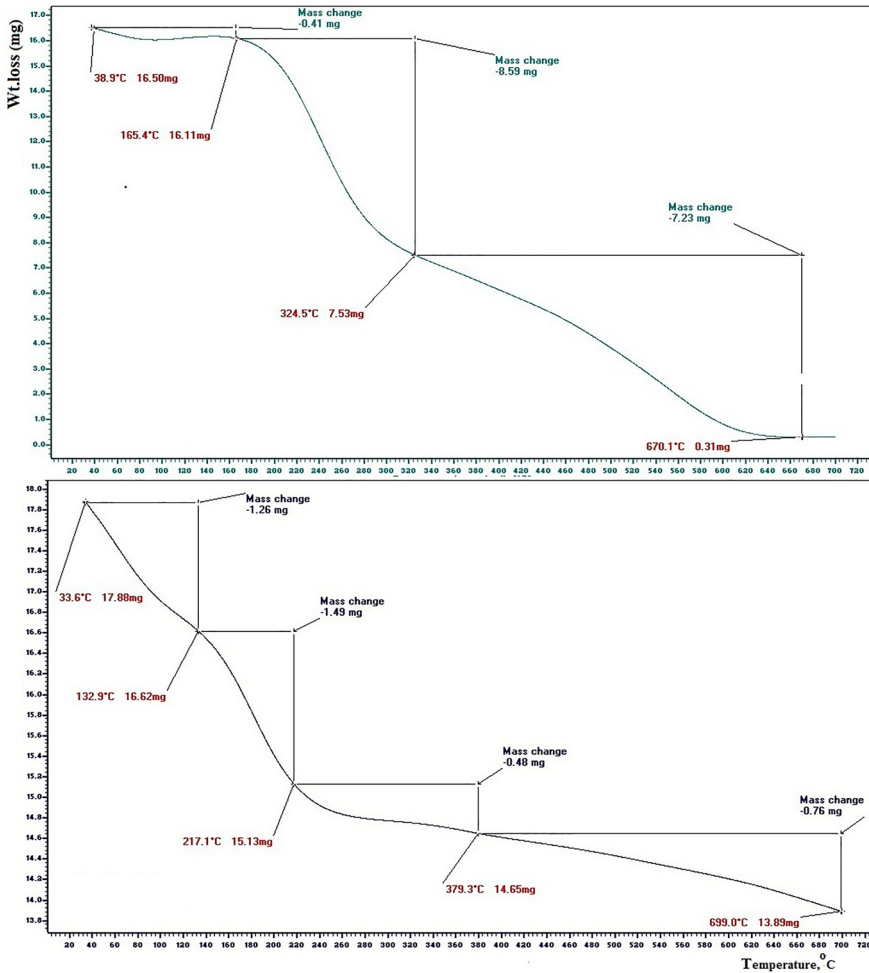


Fig. 13 TGA thermograms

Small SSE confirmed validity of pseudo-second-order kinetic model for fitting adsorption data due to good agreement between  $q_{e,exp.}$  and  $q_{e.cal.}$ . The value of  $\chi^2$  0.008 less than 0.05 confirmed neglecting null hypothesis ( $H_0$ ) and accepting hypothesis ( $H$ ) that  $q_e$  is significantly affected by contact time.

Point pH of zero point charge ( $pH_{zpc}$ ) for montmorillonite, MMT clay is determined following the method reported elsewhere [20–26]. Figure 18 shows clay MMT carries zero charge at pH 3. Below this pH, MMT carries positive charges of proton. Above this pH, clay carries negative charge of hydroxyl ion.

Stepwise hydration of interlayer cation in MMT enabled intercalation with positively charged molecules.

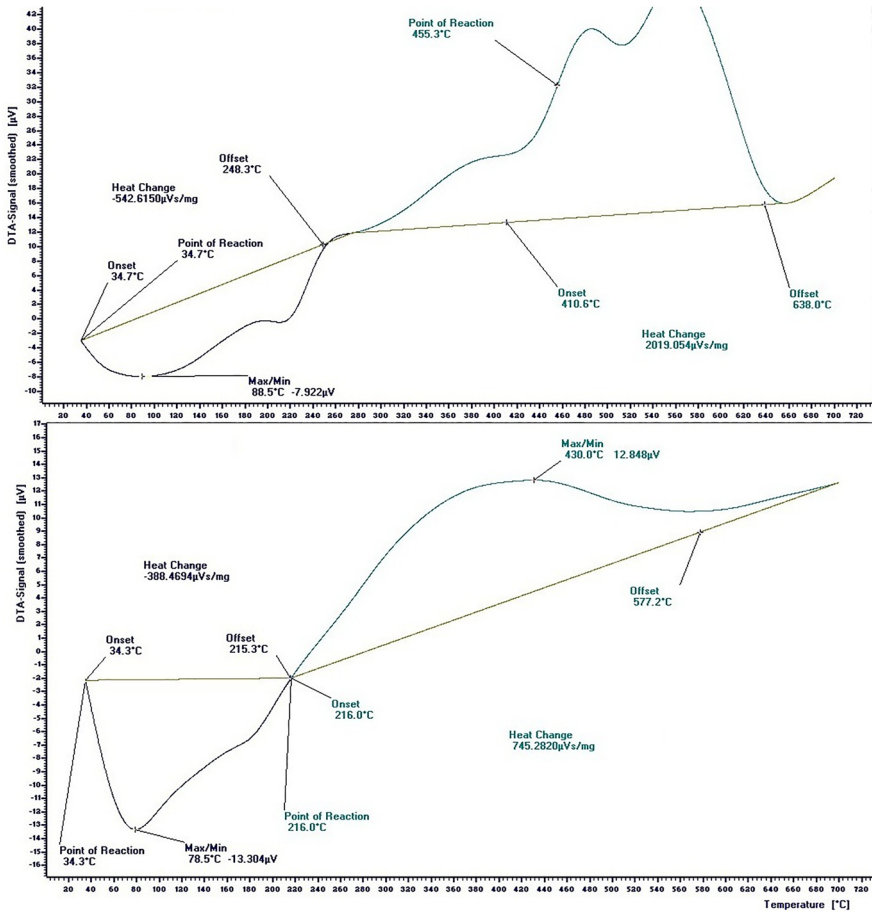
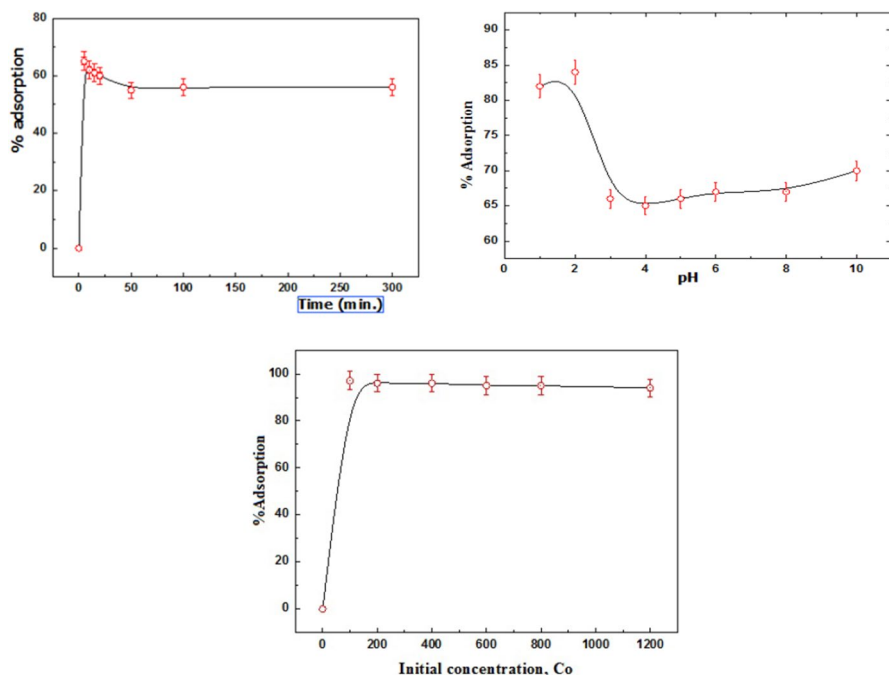


Fig. 14 DTA thermograms

BAAT is a heterocyclic compounds contains high electron density. At pH 4, BAAT is intercalated to MMT by electron donation chemisorption with no electrostatic interaction. At pH 2, BAAT linked MMT by both chemisorption and physisorption.

Although many adsorbents are reported for removal several pollutants from aqueous solution: Cd<sup>+2</sup> and Pb<sup>+2</sup> [20, 21], Cr(VI) ion [22–24, 24–29]; pb(II) ions [30, 31], reactive dyes [32, 33], MMT clay bisorbent for adsorption of 5-[4-bromobenzylidene amino)-1, 3, 4-thiadiazole-2-thiol (BATT) is not reported yet, ecofriendly and keeping environmental safety, biodegradability, availability, etc.

MMT clays are low-cost adsorbents clays keeping environment by loading various. Good adsorbent as negative charge on framework is neutralized by adsorption positively charged cations. Clay minerals such as MMT, vermiculite, illite, caulinite and bentonite adsorbents for heavy metals are low cost than activated carbon, natural and synthetic zeolites and ion-exchange resins. MMT has excellent physicochemical



**Fig. 15** Effect of contact time, pH and initial concentration on percent adsorption

properties. Clays are used: as barriers to avoid contamination of underground water and soil, preparations nanofillers and nanocomposites organic polymers. MMT clay is a bioactive glass hard solid material contains  $\text{SiO}_2$ . Bioactivity depends on various proportions and available. Silicate-rich layer is produced in human fluids such as blood. MMT is safely applied in medicine for craniofacial. MMT clay is a nature-inspired layered clay mineral. Medical MMT clay is smectite phyllosilicates clays contains  $\text{Al-O}$  and  $\text{Al(OH)}_3$  octahedral (Oh) sheet sandwiched by 2  $\text{Si-O}$

**Table 7** Thermodynamic parameters of thermal decomposition

Sample	Peak number and type	$n$	$A$	$T_m, K$	$E_a, \text{kJ mol}^{-1}$	$Z, \text{S}^{-1}$	$-\Delta S, \text{J K}^{-1} \text{mol}^{-1}$
BATT	1, Endo	2.27	0.475	362	13.15	0.004	310.82
	2, Endo	0.89	0.653	487	31.05	0.008	308.63
	3, Exo	1.52	0.553	758	81.62	0.013	307.95
	4, Exo	1.14	0.607	789	88.92	0.014	307.91
$\text{NC}_1$	1, Endo	2.46	0.460	352	25.90	0.009	304.72
	2, Exo	1.43	0.565	703	46.14	0.008	311.44

High  $E_a$  for thermal decomposition of  $\text{NC}_1$  steps 1 and 2 confirmed more thermal stability than BATT. Values of  $\Delta S$  are negative and are nearly equal indicating associative ordering mechanism of thermal decomposition

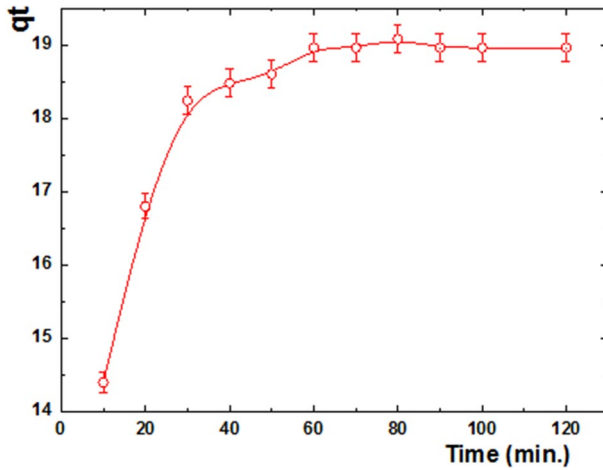


Fig. 16 Variation of adsorbed amount qt with time

Table 8 Adsorption parameters of BATT on MMT

Adsorption isotherm	Isotherm parameter	
Freundlich	$1/n$	10.86
	$K_f$	38.106
	$R^2$	0.955
	MSE	0.301
	Tempkin	$A_t$ (L/mg)
$B$		1598
$b$ (kJ/mol)		1.5504
$R^2$		0.966
MSE		0.296
D-R-	$Q_m$ (mg/g)	492.74
	$K$ (mol <sup>2</sup> /kJ <sup>2</sup> )	0.0005
	$E$ (kJ mol <sup>-1</sup> )	31.623
	$R^2$	0.980
	MSE	0.019
Halsey	$1/n_H$	10.86
	$K_H$	1.1566
	$R^2$	0.955
	MSE	0.301

tetrahedral (Td) sheets. Triple layers sheets 2:1 layer structure are bound together by Van der Waals forces. Layer thickness 1.0 nm. Lateral layers dimensions from 100 to 1000 nm. Si<sup>+4</sup> and Al<sup>+3</sup>cations exist in Td sheet. Al<sup>+3</sup>, Fe<sup>+3</sup>, Mg<sup>+2</sup> Oh sheet. Si<sup>+4</sup> substitution in both Td octahedral sheets by Al<sup>+3</sup> ion, [1–5].

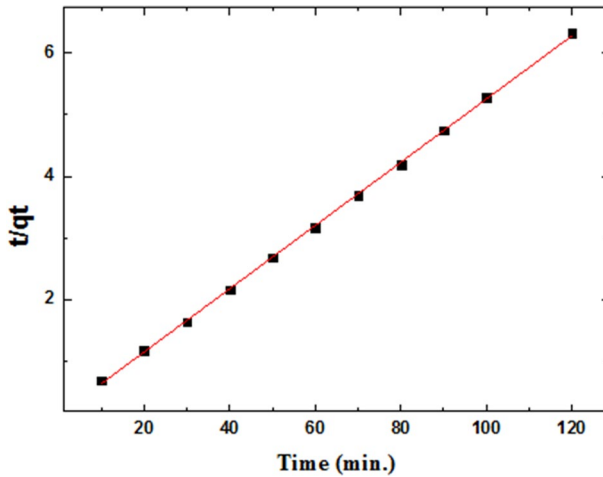


Fig. 17 Linear fitting of adsorption data to second-order kinetic model

**Table 9** Kinetic parameters of pseudo-second-order model for adsorption of AR8 on BATT

$k_2$ (g mg <sup>-1</sup> min <sup>-1</sup> )	$q_{e \text{ exp}}$ (mg g <sup>-1</sup> )	$q_{e \text{ cal}}$ (mg g <sup>-1</sup> )	$R^2$	SSE	$\chi^2$
$14.6 \times 10^{-3}$	18.9	19.3	0.999	0.16	0.008

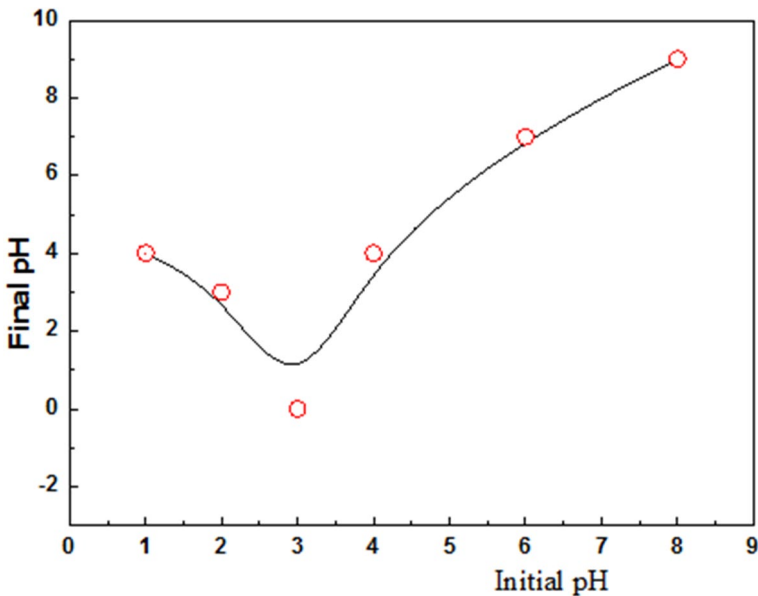


Fig. 18 pH of zero charge of clay MMT

## Conclusion

Clay montmorillonite (MMT) inorganic macromolecule is a biodegradable inert polymer carrier for biologically active and antitumor BATT heterocyclic compound. The compound showed potent antitumor activity to breast cancer and is successfully loaded on MMT clay biopolymer. Intercalation of BATT to MMT enhanced largely the electron donation capability. NC<sub>1</sub> prepared at pH 4 showed better performance and it is followed up. Poor performance of NC<sub>2</sub> prepared at pH 2 is attributed to self-assembled NPs. MMT is efficient adsorbent for BAAT to formulate drug delivery system for treating breast cancer. Results of thermodynamic and kinetic of adsorption suggested MMT are new promising bioadsorbent for therapeutic drugs.

**Supplementary Information** The online version contains supplementary material available at <https://doi.org/10.1007/s00289-022-04526-2>.

**Acknowledgements** Authors express their appreciation and acknowledgement to Alexandria University for facilitating fund provided by Science, Technology & Innovation Funding Authority (STDF) cooperated with Egyptian Knowledge Bank, EKB.

**Funding** Open access funding provided by The Science, Technology & Innovation Funding Authority (STDF) in cooperation with The Egyptian Knowledge Bank (EKB). Open access funding was provided by Science, Technology & Innovation Funding Authority (STDF, Science and Technology Development fund) in cooperation with The Egyptian Knowledge Bank (EKB). Funding was provided by Alexandria University.

**Availability of data and materials** All data and materials of study are available in manuscript and SI.

## Declarations

**Conflict of interest** Authors have declared There is no conflict of interest about publishing this manuscript.

**Consent to participate** Authors approved consent on participation.

**Consent for publication** Authors approved consent on publication.

**Ethical approval** No ethical issue in manuscript.

**Open Access** This article is licensed under a Creative Commons Attribution 4.0 International License, which permits use, sharing, adaptation, distribution and reproduction in any medium or format, as long as you give appropriate credit to the original author(s) and the source, provide a link to the Creative Commons licence, and indicate if changes were made. The images or other third party material in this article are included in the article's Creative Commons licence, unless indicated otherwise in a credit line to the material. If material is not included in the article's Creative Commons licence and your intended use is not permitted by statutory regulation or exceeds the permitted use, you will need to obtain permission directly from the copyright holder. To view a copy of this licence, visit <http://creativecommons.org/licenses/by/4.0/>.

## References

1. Fetouh HA, Ismail AM, Hamid HA, Bashier MO (2019) Synthesis of promising nanocomposites from an antitumor and biologically active heterocyclic compound uploaded by clay and chitosan polymers. *Int J Biol Macromol* 137:1211–1220

2. Fenton OS, Olafson KN, Pillai PS, Mitchell MJ, Langer R (2018) Advances in biomaterials for drug delivery. *Adv Mater* 30(29):1705328
3. Siegel RL, Miller KD, Jemal A (2020) Cancer statistics, 2020. *CA Cancer J Clin* 70(1):7–30
4. Waks AG, Winer EP (2019) Breast cancer treatment: a review. *JAMA* 321(3):288–300
5. El-Mossalamy EH, Batouti ME, Fetouh HA (2021) The role of natural biological macromolecules: deoxyribonucleic and ribonucleic acids in the formulation of new stable charge transfer complexes of thiophene Schiff bases for various life applications. *Int J Biol Macromol* 193:1572–1586
6. Alwan SM (2012) Synthesis and preliminary antimicrobial activities of new arylideneamino-1, 3, 4-thiadiazole-(thio/dithio)-acetamido cephalosporanic acids. *Molecules* 17(1):1025–1038
7. Taha AA, Shaban SM, Fetouh HA, Taha ST, Sabet VM, Kim DH (2021) Synthesis and evaluation of nonionic surfactants based on dimethylaminoethylamine: electrochemical investigation and theoretical modeling as inhibitors during electropolishing in-ortho-phosphoric acid. *J Mol Liq* 328:115421
8. Sallam ER, Khairy HM, Elnouby MS, Fetouh HA (2021) Sustainable electricity production from seawater using *Spirulina platensis* microbial fuel cell catalyzed by silver nanoparticles-activated carbon composite prepared by a new modified photolysis method. *Biomass Bioenerg* 148:106038
9. Elbatouti M, Fetouh HA (2019) Extraction of eco-friendly and biodegradable surfactant for inhibition of copper corrosion during acid pickling. *Adsorpt Sci Technol* 37(7–8):649–663
10. Unuabonah EI, Omorogie MO, Oladoja NA (2019) Modeling in adsorption: fundamentals and applications. In: *Composite nanoadsorbents*. Elsevier, pp 85–118
11. Jeon S, Clavdetscher J, Lee DK, Chankeshwara SV, Bradley M, Cho WS (2018) Surface charge-dependent cellular uptake of polystyrene nanoparticles. *Nanomaterials* 8(12):1028
12. Keshk RM, Elgawad GEA, Sallam ER, Alsubaie MS, Fetouh HA (2022) Synthesis and characterization of nicotinonitrile derivatives as efficient corrosion inhibitors for acid pickling of brass alloy in nitric acid. *ChemistrySelect* 7(33):e202202678
13. Daniel WW, Cross CL (2018) *Biostatistics: a foundation for analysis in the health sciences*. Wiley
14. Hosseini S, Chamani J, Hadipannah MR, Ebadpour N, Hojjati AS, Mohammadzadeh MH, Rahimi HR (2019) Nano-curcumin's suppression of breast cancer cells (MCF7) through the inhibition of cyclinD1 expression. *Breast Cancer Targets Ther* 11:137
15. Nazmutdinov RR, Ulstrup J (2021) Retrospective and prospective views of electrochemical electron transfer processes: theory and computations. *At Scale Model Electrochem Syst* 25–91
16. Fetouh HA, Abd-El-Nabey BA, Goher YM, Karam MS (2018) An electrochemical investigation in the anticorrosive properties of silver nanoparticles for the acidic corrosion of aluminium. *J Electrochem* 24(1):89
17. Mailoud OM, Elsayed AH, El Fetouh HA, ELazm AA (2019) Synthesis and characterization of paramagnetic isotropic glycine manganese chloride single crystal with various dopant concentrations. *Results Phys* 12:925–933
18. González-López ME, Laureano-Anzaldo CM, Pérez-Fonseca AA, Arellano M, Robledo-Ortíz JR (2021) A critical overview of adsorption models linearization: methodological and statistical inconsistencies. *Sep Purif Rev* 1–15
19. Fetouh HA, Hefnawy A, Attia AM, Ali E (2020) Facile and low-cost green synthesis of eco-friendly chitosan-silver nanocomposite as novel and promising corrosion inhibitor for mild steel in chilled water circuits. *J Mol Liq* 319:114355
20. Kuncoro EP, Isnadina DRM, Darmokoesoemo H, Dzembarahmatiny F, Kusuma HS (2018) Characterization and isotherm data for adsorption of  $Cd^{2+}$  from aqueous solution by adsorbent from mixture of bagasse-bentonite. *Data Brief* 16:354–360
21. Kuncoro EP, Isnadina DRM, Darmokoesoemo H, Fauziah OR, Kusuma HS (2018) Characterization, kinetic, and isotherm data for adsorption of  $Pb^{2+}$  from aqueous solution by adsorbent from mixture of bagasse-bentonite. *Data Brief* 16:622–629
22. Neolaka YA, Supriyanto G, Darmokoesoemo H, Kusuma HS (2018) Characterization, kinetic, and isotherm data for Cr (VI) removal from aqueous solution by Cr (VI)-imprinted poly (4-VP-co-MMA) supported on activated Indonesia (Ende-Flores) natural zeolite structure. *Data Brief* 17:969–979
23. Neolaka YA, Supriyanto G, Darmokoesoemo H, Kusuma HS (2018) Characterization, isotherm, and thermodynamic data for selective adsorption of Cr (VI) from aqueous solution by Indonesia (Ende-Flores) natural zeolite Cr (VI)-imprinted-poly (4-VP-co-EGDMA)-ANZ (IIP-ANZ). *Data Brief* 17:1020–1029
24. Neolaka YA, Lawa Y, Naat J, Riwu AA, Lindu YE, Darmokoesoemo H, Widyaningrum BA, Iqbal M, Kusuma HS (2021) Evaluation of magnetic material IIP@ GO- $Fe_3O_4$  based on Kesambi wood



- (Schleichera oleosa) as a potential adsorbent for the removal of Cr (VI) from aqueous solutions. *React Funct Polym* 166:105000
25. Neolaka YA, Lawa Y, Naat J, Riwu AA, Mango AW, Darmokoesoemo H, Widyaningrum BA, Iqbal M, Kusuma HS (2022) Efficiency of activated natural zeolite-based magnetic composite (ANZ-Fe<sub>3</sub>O<sub>4</sub>) as a novel adsorbent for removal of Cr (VI) from wastewater. *J Market Res* 18:2896–2909
  26. Neolaka YA, Supriyanto G, Kusuma HS (2018) Adsorption performance of Cr (VI)-imprinted poly (4-VP-co-MMA) supported on activated Indonesia (Ende-Flores) natural zeolite structure for Cr (VI) removal from aqueous solution. *J Environ Chem Eng* 6(2):3436–3443
  27. Neolaka YA, Lawa Y, Naat JN, Riwu AAP, Darmokoesoemo H, Supriyanto G, Holdsworth CI, Amenaghawon AN, Kusuma HS (2020) A Cr (VI)-imprinted-poly (4-VP-co-EGDMA) sorbent prepared using precipitation polymerization and its application for selective adsorptive removal and solid phase extraction of Cr (VI) ions from electroplating industrial wastewater. *React Funct Polym* 147:104451
  28. Neolaka YA, Lawa Y, Naat JN, Riwu AA, Iqbal M, Darmokoesoemo H, Kusuma HS (2020) The adsorption of Cr (VI) from water samples using graphene oxide-magnetic (GO-Fe<sub>3</sub>O<sub>4</sub>) synthesized from natural cellulose-based graphite (kusambi wood or Schleichera oleosa): study of kinetics, isotherms and thermodynamics. *J Market Res* 9(3):6544–6556
  29. Budiana IGMN, Jasman J, Neolaka YA, Riwu AA, Elmsellem H, Darmokoesoemo H, Kusuma HS (2021) Synthesis, characterization and application of cinnamoyl C-phenylcalix [4] resorcinarene (CCPCR) for removal of Cr (III) ion from the aquatic environment. *J Mol Liq* 324:114776
  30. Naat JN, Neolaka YA, Lapailaka T, Tj RT, Sabarudin A, Darmokoesoemo H, Kusuma HS (2021) Adsorption of Cu (II) and Pb (II) using silica@ mercapto (hs@ m) hybrid adsorbent synthesized from silica of Takari sand: optimization of parameters and kinetics. *Rasayan J Chem* 14(1):550–560
  31. Neolaka YA, Lawa Y, Naat J, Riwu AA, Darmokoesoemo H, Widyaningrum BA, Iqbal M, Kusuma HS (2021) Indonesian Kesambi wood (Schleichera oleosa) activated with pyrolysis and H<sub>2</sub>SO<sub>4</sub> combination methods to produce mesoporous activated carbon for Pb (II) adsorption from aqueous solution. *Environ Technol Innov* 24:101997
  32. Aigbe UO, Ukhurebor KE, Onyancha RB, Osibote OA, Darmokoesoemo H, Kusuma HS (2021) Fly ash-based adsorbent for adsorption of heavy metals and dyes from aqueous solution: a review. *J Market Res* 14:2751–2774
  33. Batouti ME, Sadik W, Eldemerdash AG, Hanafy E, Fetouh HA (2022) New and innovative microwave-assisted technology for synthesis of guar gum-grafted acrylamide hydrogel superabsorbent for the removal of acid red 8 dye from industrial wastewater. *Polym Bull* 1–25

**Publisher's Note** Springer Nature remains neutral with regard to jurisdictional claims in published maps and institutional affiliations.